



Full length article

A spall and diffraction study of nanosecond pressure release across the iron ϵ - α phase boundary

Gaia Righi^{a,*}, Richard Briggs^a, Orlando R. Deluigi^b, Camelia V. Stan^a, Saransh Singh^a, Samantha M. Clarke^a, Eduardo M. Bringa^b, Raymond F. Smith^a, Robert E. Rudd^a, Hye-Sook Park^a, Marc A. Meyers^c

^a Lawrence Livermore National Laboratory, Livermore, CA 94550, USA

^b CONICET and Universidad de Mendoza, M5500 Mendoza, Argentina

^c University of California, San Diego, La Jolla, CA 92093, USA



ARTICLE INFO

Keywords:

Iron
High pressure
Spall
X-ray diffraction
Phase transformation
Molecular Dynamics

ABSTRACT

The extreme response of polycrystalline iron at high pressures and high strain rates is revealed by means of high-power laser pulses. The compression portion of the pulse coupled with x-ray diffraction identifies the expected body-centered cubic (α) to hexagonal close packed (ϵ) displacive transformation. Upon release, observation shows that the complete reverse transformation takes approximately 8 ns and that the structure returns to its initial microstructural configuration, in a reversible transformation path. This is in good agreement with molecular dynamics (MD) simulations which predict an inverse dependence between transformation time and strain rate. The grain size is reduced from μm to nm range during compression and begins increasing back to the original grain size on decompression. The kinetics of the transition is dictated by heterogeneous nucleation as it follows the Johnson-Mehl-Avrami-Kolmogorov equation with the appropriate time exponent of ~ 1 . This is confirmed by MD simulations which also identify profuse twinning and dislocation generation. The tensile pulse generated upon reflection at the free surface is captured by time-resolved free surface velocity measurements from which a peak tensile stress of 7 GPa is obtained, in stark contrast with its quasi-static value of ~ 200 MPa. At these strain rates, the strength of grain interiors, which is determined by twinning and slip exceeds the strength of the boundaries, and failure initiates preferentially in the latter.

1. Introduction

The high-pressure behavior of iron (Fe) has been extensively studied over the past seven decades. In particular, there have been numerous experimental studies on the α - ϵ (body-centered cubic (BCC) to hexagonal close-packed (HCP)) phase transition in iron both through static [1–9] and dynamic methods [10–15]. Under shock compression, this phase transformation occurs at ~ 13 GPa [16] through non-diffusive, martensitic reordering of atomic planes [17] and is strongly influenced by deformation twinning [18]. Furthermore, this phase transition has been found to affect the extent of damage that occurs during dynamic fracture, or spallation [19,20]. When iron is spalled with lower pressure shocks, below the α - ϵ phase transition, the observed failure was brittle – dominated by crack initiation and growth. However, if the material is shocked to higher pressure, above the transition into the ϵ

phase, the spalled surface is dimpled (i.e., ductile failure) – dominated by void nucleation and growth. Prior to complete spall, there is a release stage in which the large compressive stress decreases due to wave interactions with the free surface. This causes the high-pressure ϵ phase to transform back to the ambient α phase [19,21]. This reversion to the ambient crystal structure has also been found to be accompanied by a restoration of the original microstructure [22–24]. The multiple HCP variants that form from the compression and shuffling of BCC planes are what lead to a breakup of the microstructure, down to 10's of nanometers [17]. After the passage of a rarefaction wave, HCP planes expand and return to their ambient positions for the new lower pressure BCC state. Interestingly, it has been found that this reverse pathway follows the forward (α - ϵ) pathway and, thus, causes the grains to retransform to their original variant [24]. There is both an atomistic and microstructural memory effect during shock compression and release of iron.

* Corresponding author.

E-mail address: righi1@llnl.gov (G. Righi).

<https://doi.org/10.1016/j.actamat.2023.119148>

Received 16 February 2023; Received in revised form 15 May 2023; Accepted 8 July 2023

Available online 10 July 2023

1359-6454/© 2023 Acta Materialia Inc. Published by Elsevier Ltd. All rights reserved.

Many studies have focused on the pressure hysteresis of these phase transitions under static, diamond anvil cell loading [2–6,9]. All these studies are in agreement that the α - ϵ transition begins at 13 ± 4 GPa and completes around 18 GPa while the reverse, ϵ - α , transition begins around 10 GPa and completes around 5 GPa. The kinetics of the α - ϵ phase transition is also well studied, both experimentally [21,25–27] and computationally (shock propagation in single [14,26,28,29] and polycrystals [30–32], uniaxial compression [33–36]), but is not the focus of this work. Here, we instead focus on the timescale and microstructural effects of the ϵ - α transformation following shock compression and pressure release, a phenomenon that has been rarely studied. There are only a few atomistic simulation studies covering this regime [29,30,35,37]. With a better understanding of the atomic- and micro-scale processes that occur prior to and during dynamic failure, constitutive and failure models can be improved to better predict impact and failure events. At extremely high strain rates of 10^9 s^{-1} , the HCP phase in small-grained iron was found to disappear over approximately 200 ps [22]. MD of the reverse (ϵ - α) transformation at strain rate of 10^9 s^{-1} found a transformation time of ~ 170 ps [33] and that the formation of twins played an important role in spall strength [29]. Here and throughout, strain rate refers to the total uniaxial release strain rate, $-\dot{V}/V_0$. The processes that occur prior to complete spall dictate the mode of failure. The rapidity of the atomic-level changes is just the first step in how quickly the microstructure will subsequently evolve. How the microstructure changes will then have a profound effect on the type of failure and, consequently, how much damaging debris will form.

High-intensity lasers paired with high-energy x-rays provide a unique capability to study phase transition dynamics in iron. The various phenomena connected to shock release due to wave interactions at a free surface (spall strength, ϵ - α transition timescale, and microstructural evolution) are investigated both experimentally and computationally. MD simulations under uniaxial compression-release are used

to compare experimental results of strain rate and ϵ - α transformation time. Furthermore, MD simulations are used to show the evolution of the atomic structure during compression and unloading. To the authors' knowledge, there has never been such a detailed study of the shock-induced reverse phase transformation in iron that ties together time-resolved experiments with atomic-scale modeling to fully understand spall failure. In this work, we present a detailed study of the shock-induced reverse phase transformation in iron, combining time-resolved experiments with atomic-scale modeling to fully understand spall failure.

2. Experimental and Computational Methods

Laser shock experiments were conducted at the Dynamic Compression Sector (DCS) of the Advanced Photon Source (APS) in Argonne National Laboratory [38]. Time-resolved x-ray diffraction (XRD) was performed using an x-ray beam with focal spot size of $\sim 50 \mu\text{m}$ from a ~ 23.5 keV pink beam source [39]. Scattered x-rays were recorded on a Rayonix SX165 detector 97.7 mm from the sample. A nominally 100 J (~ 80 J at 351 nm) laser with a 1 mm spot size and 10 ns pulse length was used to generate a shock wave in the target package. Targets consisted of a $30 \mu\text{m}$ polystyrene ablator glued onto ~ 50 - $70 \mu\text{m}$ polycrystalline iron foils using Hardman Double Bubble epoxy (Fig. 1a). Grain sizes were found to be $5 \mu\text{m}$ along the shock direction and 100 - $250 \mu\text{m}$ normal to the shock direction (determined using Electron Backscatter diffraction as part of a complementary study [40]). Point [41] and line [42] velocity interferometer system for any reflector (VISAR) were used to record free surface velocity (Fig. 1b), which was used to calculate the peak pressure, strain rate, and spall strength. Pre-shot hydrodynamic simulations were performed using Hydra [43] to determine the x-ray timing for structural characterization the iron samples on compression ($t < 0$ ns) or on release ($t > 0$ ns), where 0 ns refers to the shock arrival time at the rear surface

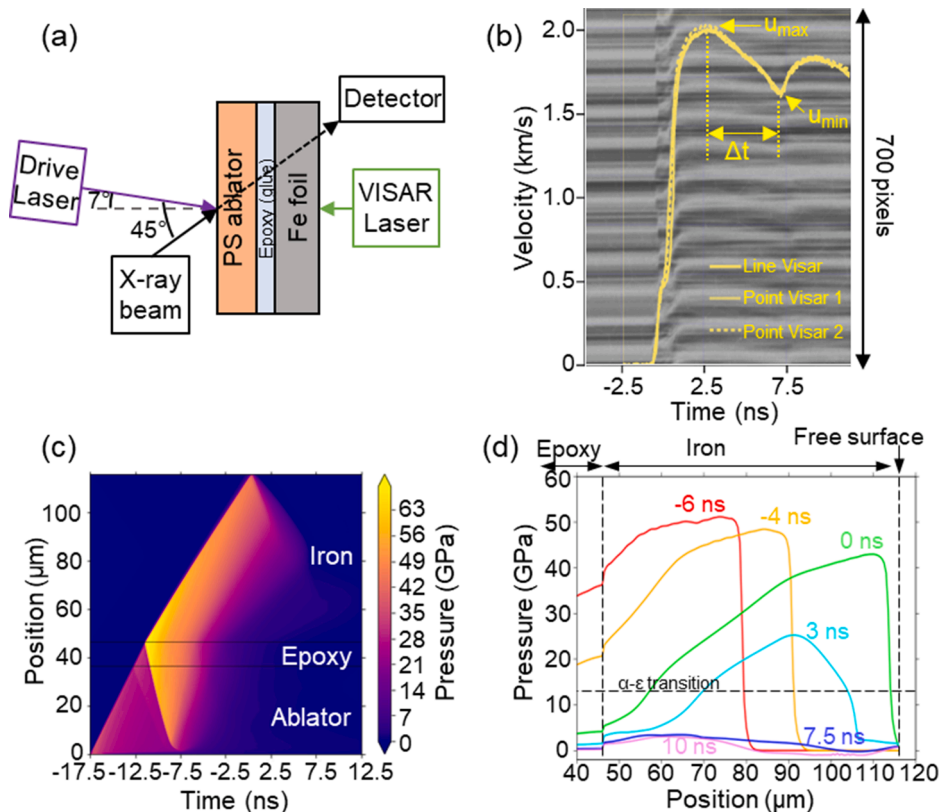


Fig. 1. (a) Experimental set-up (not to scale) and (b) representative VISAR data (solid line represents line VISAR and dashed lines represent two channels of point VISAR). U_{max} , U_{min} , and Δt values of 1.99 km/s, 1.62 km/s, and 4.3 ns correspond to strain rate and spall strength of $7.24 \times 10^6 \text{ s}^{-1}$ and 8.87 GPa. (c) Position-time (x-t) plot of pressure from Hydra simulations and (d) corresponding lineouts of pressure as a function of position within the iron at various time points.

of the iron sample. Post-shot hydrodynamic simulations were also performed with Hydra [43], using the as-delivered laser power-time profile to understand the pressure profile in the iron sample achieved during the experiment (Fig. 1c-d). The shock pressure is high enough to overdrive the forward α - ϵ phase transformation, resulting in a single-shock loading. Dioplas [44] was used to calibrate the sample-detector distance using ceria (CeO_2) and silicon x-ray standards and to azimuthally integrate x-ray patterns. GSAS-II software [45] was used to obtain structural information from the integrated x-ray diffraction patterns. An instrument parameter file was created using the CeO_2 standard, which defines the inherent peak broadening and peak shape of the pink beam (from [39]). These instrument parameters were then used for fitting of the unshocked, shocked, and released phases.

Molecular dynamic simulations of uniaxial compression were carried out using LAMMPS [46]. BCC Fe polycrystals were modeled with an embedded atom method (EAM) potential developed by Gunkelmann and co-workers [36]. This potential is widely used due to its ability to adequately reproduce the α - ϵ transition [28,29,33,34,37,40], avoiding some limitations of previous EAM potentials [35,36]. Polycrystal samples were designed using Atomsk [47] with dimensions of $(100a_0)^3$, leading to 2 million atoms in 30 grains, with a mean grain diameter ~ 7 nm. Samples were compressed up to 15% strain along [001] at strain rates of $2 \times 10^7 \text{ s}^{-1}$, 10^8 s^{-1} , and 10^9 s^{-1} and held at this maximum strain for 20 ps. Finally, samples were unloaded by applying uniaxial tension along the same axis at the same strain rate, to achieve zero uniaxial strain and stress by the end of the simulations under NVE (number, volume, energy) ensemble. This procedure is often used [33–36] as an alternative to much larger wave-propagating simulations. All samples were created with periodic boundary conditions (PBC) and annealed at 300 K and zero pressure prior to compression. Sample with ~ 5 million atoms (30 grains, mean grain diameter ~ 15 nm) at 300 K and 2 million atoms at 700 K (30 grains, mean grain diameter ~ 7 nm) were also simulated to compare back transformation time. Visualization and analysis were performed using OVITO [48]. Crystal structure was identified with Polyhedral Template Matching (PTM) [49], a robust method to identify structures at high temperatures and pressures, using root-mean-square deviation (RMSD) equal to 0.1. Dislocations were analyzed with the Dislocation Extraction Algorithm (DXA) in OVITO [48].

3. Results and Discussion

X-ray diffraction measurements were taken using a 100 ps x-ray exposure at different delay times with respect to shock breakout, which is defined as $t = 0$ ns. The delay times were chosen based on pre-shot hydrodynamic simulations to capture the iron at different states of compression and release. The location and time point of the spallation event can be determined from the x-t plot in Fig. 1c by finding the intersection of the free surface and drive side release waves. In this case, the spall plane is about halfway into the iron, at $\sim 80 \mu\text{m}$. Two complementary velocimetry systems (point-VISAR [41] and line-VISAR [42]) were used to measure the velocity of the free surface which is used to characterize the shocked state of the samples. By adjusting the delay time while keeping laser and sample parameters approximately constant, time-resolved phase information on the shock compression and release behavior of iron was obtained.

Free surface velocity profiles from experimental data were used to calculate strain rate and spall strength at failure. The peak free surface velocity, u_{max} , and the spall pullback signal, u_{min} , (Fig. 1b) in a simplified acoustic approach yields the following approximation for strain rate [50]

$$\dot{\epsilon} = \frac{(u_{max} - u_{min})}{\Delta t \times 2c} \quad (1)$$

where Δt is the time difference between u_{max} and u_{min} and c is the sound

velocity on release (6 km/s [51]). The spall strength can be calculated using a similar acoustic approximation

$$P_{spall} = (1/2)\rho_0 c(u_{max} - u_{min}) \quad (2)$$

where ρ_0 is the initial density. Peak pressure was calculated using the Hugoniot relationship between pressure and particle velocity (u_p) assuming $u_{max} \approx 2u_p$. For the calculated data presented here, values in parenthesis represent standard deviation due to variation in sample thickness (30 – 70 μm) and laser power (70 – 73 J). The average peak pressures and strain rates achieved in the samples were 56 (7) GPa and $8.7 (3.9) \times 10^6 \text{ s}^{-1}$, respectively. According to Hydra modeling using the equation of state LEOS 260, the ranges of internal pressure, temperature, and strain rate (depending on the position within the iron) are 45 – 60 GPa, 800 – 1200 K, and $8 - 15 \times 10^6 \text{ s}^{-1}$, respectively. It is important to note that there is also a release wave that originates from the drive side due to the cessation of laser irradiation; however, this release is at a reduced rate and magnitude compared to release from the free surface. This combination of release waves contributes to the large range of pressures, temperatures, and strain rates within the sample predicted from modeling. However, the simulated values for pressure and strain rate are similar to the calculated values from free surface velocity measurements. Temperature is not directly measured. The average spall strength for these polycrystalline samples was found to be 7.5 (1.1) GPa. The spall strength observed here is in close agreement with values found in other laser shock work [20,40,52] (Fig. 2) and this suggests similar failure mechanisms (i.e., ductile fracture). The grain boundaries in polycrystalline materials act as preferential void nucleation and dislocation pile-up locations under tensile and shear loading [53]. Grain boundaries, in conjunction with the α - ϵ - α phase transition cycle, cause ductile failure due to void formation and growth and, ultimately, failure along boundaries. This failure behavior is typical of BCC metals like tantalum [54] and vanadium [55]. It should be mentioned that the spall strength has a significant strain rate dependence. In gas gun experiments, where the pulse duration is in the μs domain, the spall strength is around 2 GPa [56].

By adjusting the x-ray timing for each shot, without changing the

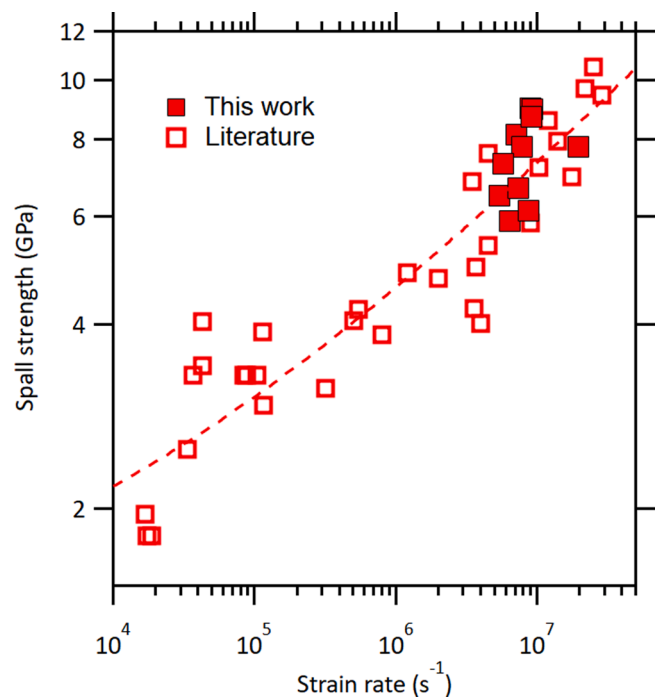


Fig. 2. Spall strength comparison from experiments described here (filled squares) and literature [20,40,52,56–60] (open squares). Dashed line represents fit to $P_{spall} \sim \dot{\epsilon}^{1/4}$ as previously observed in Kanel et al. [61].

laser energy, time-resolved phase transformation data were collected. The known ambient (BCC: $Im\bar{3}m$) and high-pressure (HCP: $P6_3/mmc$) crystal structures of iron were used to fit the diffraction peaks seen in the x-ray data (Fig. 3). Integrated diffraction patterns from a series of shots are shown in Fig. 4a where the evolution of the crystal structure can be clearly seen. As expected, at negative times as the shock wave runs through, more iron is rapidly compressed and the ambient BCC peaks decrease in intensity as the HCP peaks grow. Around 0 ns, the integrated pattern shows little evidence of any BCC structure ($< 10\%$). As the release waves travel over the compressed material at positive times, BCC peaks begin being evident again, with less than 5% HCP structure present at the latest time point.

The reverse ε - α transformation begins rapidly – with the first signs of released BCC peaks visible at 0.85 ns after shock breakout. Over the course of shock release, the phase transition completes within ~ 8 ns, with the exact duration inconclusive due to sparsity of data points. However, the latest time point does show that 97% of the structure has retransformed to BCC. Consequently, 8 ns is a reasonable value for the time needed post breakout for essentially all of the iron to transform. We note that the 8 ns estimate is also dependent on the release wave propagation velocity through the compressed sample, so the transformation time for some material elements (closer to the release surface) is likely much shorter. As these diffraction measurements are volume-integrated, any BCC or HCP peaks are an average across the entire sample. The kinetics of the iron ε - α transformation observed here is slower than previous reports with polycrystalline iron (200 ps in Hwang et al. [22] for $\dot{\varepsilon} \approx 10^9 \text{ s}^{-1}$), but this difference is expected due to the lower strain rate of experiments described here ($10^6 - 10^7 \text{ s}^{-1}$), as discussed below from MD simulations. A similar trend in phase transition time with strain rate can be seen for the α - ε transformation during compression [14].

The volume-integrated weight fraction of BCC phase is determined using Rietveld refinement [62] with GSAS-II software, using the pink beam profile function described in Von Dreele et al. [39]. The resulting

evolution from BCC to HCP is clearly seen during compression (negative times), and the reverse transition occurs during release (positive times for material near the free surface) (Fig. 4b). The forward α - ε transformation is over-driven and fast, resulting in little structure to the shock profile in the VISAR trace (Fig. 1b), and a BCC fraction at $t < 0$ ns that is approximately equal to the fraction of material at pressures below the α - ε phase boundary according to the Hydra simulations (red circles and purple triangles in Fig. 4b). The Hydra simulations assume instantaneous transformation, which due to the drive-side release can account for the disagreement of the BCC fraction at $t \sim 0$. The kinetics of this reverse phase transformation can be further described using a simple phenomenological rate equation: the Johnson-Mehl-Avrami-Kolmogorov (JMAK) model [63–65]. This type of formulation was originally designed to describe isothermal material solidification processes but has been applied to solid-state phase changes as well [66,67]. This model describes the transformed volume fraction in an exponential form

$$Y(t) = 1 - \exp\left[-\left(\frac{t}{\tau}\right)^n\right] \quad (3)$$

where $Y(t)$ is the fraction of the material transformed as a function of time, t , $1/\tau$ is the rate constant, and n is the JMAK kinetic exponent. This exponent can provide information about the nature of the phase nucleation process where the value can vary between 1 and 4, corresponding to heterogeneous or homogeneous nucleation. The best-fit parameters for the JMAK model to our data neglecting wave propagation are $\tau = 4.17$ (0.31) ns and $n = 1.38$ (0.24). The rate constant, $K = 1/\tau$ is estimated to be 0.24 (0.02) ns^{-1} . The exponent around 1 corresponds to non-random nucleation sites and growth being restricted to 1-2 dimensions [68], i.e. grain boundary-dominated phase nucleation. A more complex form of the JMAK model may include wave propagation effects and would reduce τ .

The shock-induced changes in microstructure can also be extracted from GSAS-II analysis – primarily the grain size. The software uses typical Scherrer broadening [69] to determine grain size, so the overall

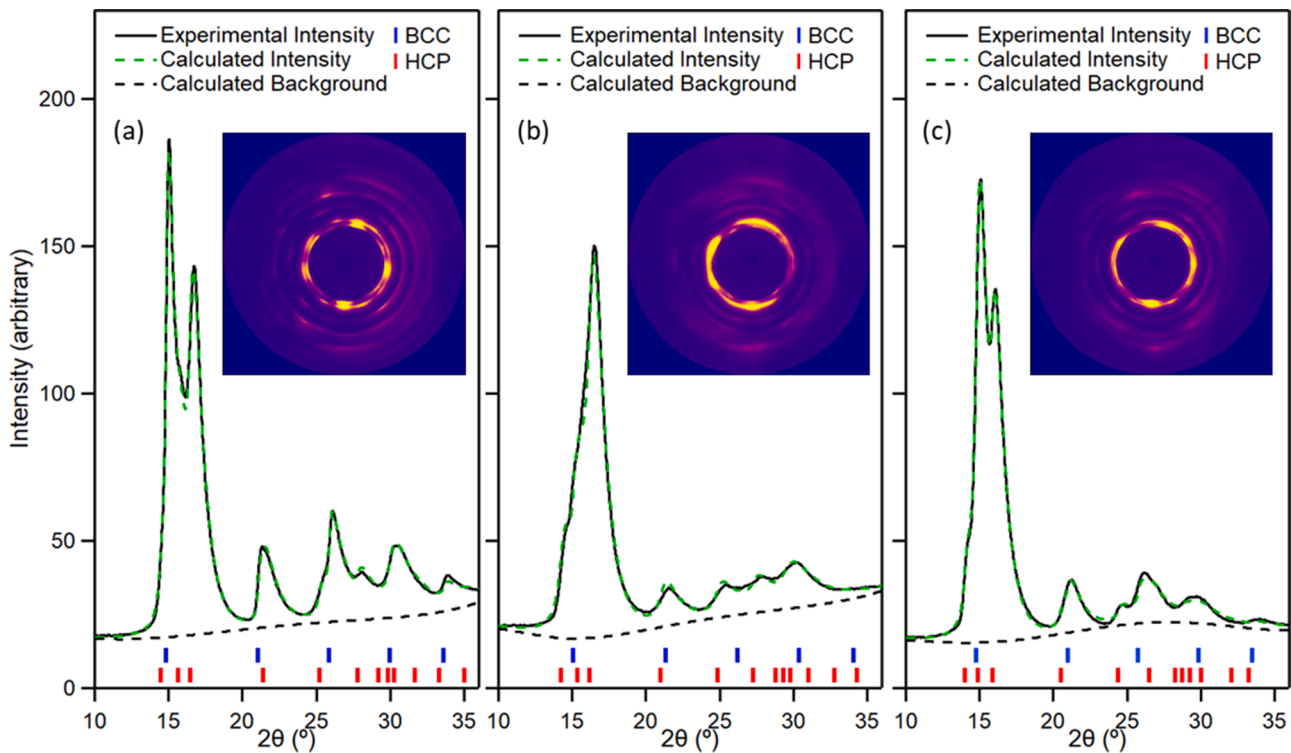


Fig. 3. Measured (black solid line) and calculated XRD profile (green dashed line) using Rietveld refinement [62] with GSAS-II software for iron at (a) -3.5, (b) 0.03, and (c) 3.03 ns. Inset shows collected diffraction data. Diffraction patterns show a combination of BCC (blue ticks) and HCP (red ticks). Note in the diffraction rings that much of the texture in (a) has returned in (c).

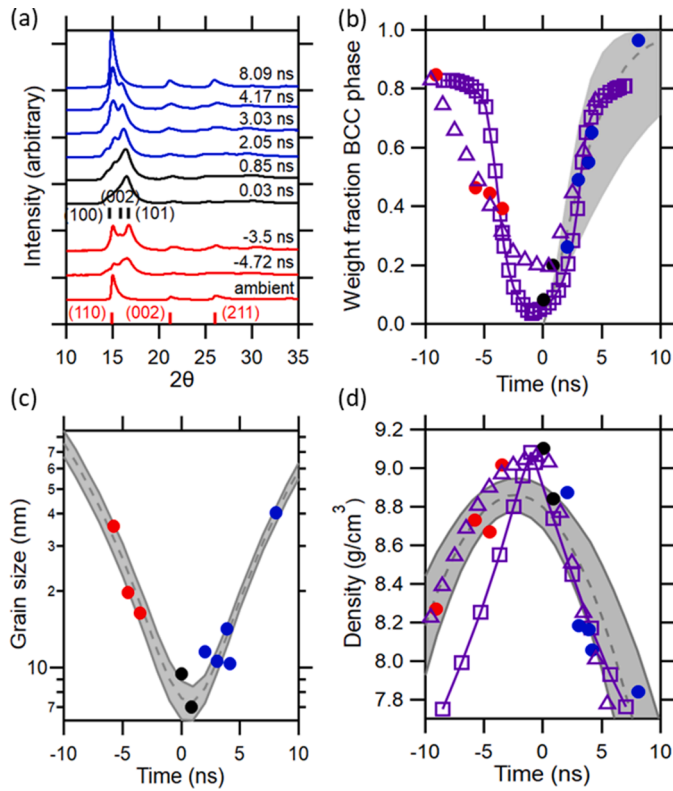


Fig. 4. (a) Waterfall plot of polycrystalline iron showing evolution of BCC and HCP peaks as x-ray timing is varied. Through-thickness averages of (b) weight fraction of BCC phase, (c) weighted grain size, and (d) weighted density as functions of x-ray timing. In (b-d) experiments are shown in filled circles (red symbolizes compressive state, black symbolizes data around shock breakout, blue symbolizes a release state) and MD (for $\dot{\epsilon} = 2 \times 10^7 \text{ s}^{-1}$) and Hydra simulations are shown in open symbols (squares and triangles, respectively). Dashed lines represent the fit with 1 standard deviation shown in shaded region.

value in the sample (Fig. 4c) is taken to be a weighted sum of the product of the weight fraction of each phase and its corresponding grain size calculated by the program. The grain size evolution shows evidence of a memory effect, with the original, large, grains reducing to sizes on the order of 10's of nanometers during compression and at later times, during release, becoming larger. This evident memory effect agrees with results found in both diamond anvil cell [9] and laser shock experiments [12,22] and can explain the dependence of grain size on spall strength found in previous work [40,52]. The reduction of grain size down to the nm-scale upon compression also agrees well with other experiments [17,23,24] and simulations [33,35] of iron microstructure at high pressure. Additional factors that can contribute to peak broadening, such as temperature and plasticity are accounted for using fitting parameters in GSAS-II (Debye-Waller factor, and microstrain, respectively). Lastly, GSAS-II was also used to determine the density of the shocked area probed by the x-ray beam (Fig. 4d). Again, the overall density is taken to be a weighted sum of the densities of each phase. As expected, during negative times the weighted density increases as the sample converts from the ambient BCC phase to the compressed, high density HCP phase. When the structure has mostly transformed to HCP iron at 0.03 ns, the density ($\sim 9.1 \text{ g/cm}^3$) is in excellent agreement with the corresponding MD simulations. Density from MD is calculated as

$$\rho = \frac{55.845}{\text{AtomicVolume} * N_A} \quad (4)$$

where ρ is the average density for all atoms in the samples (FCC, BCC, HCP and others), N_A is Avogadro's number, and the Atomic Volume is

the average atomic volume for atoms of a given structure type, obtained by performing Voronoi analysis in OVITO. It is important to note that even though the sample is at peak compression (i.e., mostly HCP), there are still a large range of pressures within the iron from both the free surface and drive side release waves. Specifically, simulations show the drive side release wave lowers the pressure of the iron sample to $\sim 20 \text{ GPa}$, whereas release from the free surface causes a drop in pressure to 0 GPa almost instantaneously. The release wave from the drive side causes a large range of densities for iron in the HCP phase (Fig. S1). This results in a weighted density that is lower than what is expected for shocked iron to $\sim 60 \text{ GPa}$. Nevertheless, the radiation hydrodynamic simulations of the experiment (Fig. 1c) predict the average density across the iron sample at breakout (i.e., 0 ns) to be $\sim 9.06 \text{ g/cm}^3$, which is also in excellent agreement with experiments and MD. As shock release from the free surface begins, the density decreases and eventually drops below ambient at late times as the crystal structure is expanded, possibly due to temperature effects [70].

The results observed in the experiments are compared with MD simulations of homogeneous uniaxial compression and release. The average peak stress obtained in MD varies between 43 and 47 GPa, similar to values calculated from VISAR, with all simulated samples presenting similar stress-strain behavior (Fig. S2a). The phase transformation starts at $\sim 7.5\%$ compression and no residual strain is seen at 0 GPa, similar to results obtained by Gunkelmann [33]. Due to imperfect grain boundary atoms, a small number of BCC and HCP atoms are identified at $\sim 15\%$ (compression) and 0% (release) strain, respectively. The pressure-volume-temperature trajectory is not along the Hugoniot, but it compares reasonably well with trajectories from much larger non-equilibrium shock simulations. Wave propagation simulations at strain rates of 10^7 s^{-1} would be difficult, even with significant supercomputing resources. Despite the differences in loading rate between the experiments and the homogeneous MD simulations, the resulting microstructure after compression is expected to be similar [29]. Fig. 4b compares the atom fraction for experimental and MD (strain rate of $2 \times 10^7 \text{ s}^{-1}$) results. A great similarity in phase evolution for ϵ - α was observed and the fit performed for the experimental values (Eq. 3) agrees reasonably well with the results obtained by MD. Note that the final weight fraction of α (BCC) iron differs between the experiment and the simulation. This could be due to difference in assumed temperature ($T \sim 800 \text{ K}$ per radiation hydrodynamic modeling versus $T \sim 550 \text{ K}$ per MD (Fig. S2b)) or change in grain morphology and other defects; the number of grains in the simulations presented here grows from 30 to 38, according to the OVITO tool Grain Segmentation Modifier [48], because of the appearance of twins during the back transformation, which lead to spurious grain splitting.

To measure the ϵ - α transformation time in the simulations, the difference between the structure at 15% and 0% strain was considered. At zero strain there are 83% BCC atoms, with the rest being disordered atoms at grain boundaries. At the largest strain, there are $\sim 3\%$ BCC atoms whereas after the structure has been released, $\sim 81\%$ atoms are recovered as BCC. The reverse transformation times are plotted as function of the strain rate (Fig. 5), where it can be said that there is a reasonable agreement between the results obtained in this experiment (8 ns) and a compression-relaxation simulation (11 ns). The differences in the reverse transformation time can be due to the differences in sample size (μm -scale versus nm-scale), strain rate (10^6 s^{-1} versus 10^8 s^{-1}), wave propagation, or assumed temperature. Furthermore, at higher strain rate there is also reasonable agreement with the HCP transformation time from Hwang et al. [22]. Finally, the transformation time was compared for samples with different initial temperature and different grain size at strain rates of 10^8 s^{-1} (Fig. S3). At higher temperature (700 K), there is a higher transformation rate during the initial stage of the ϵ - α transition, but the final phase fractions are equivalent to the lower temperature case. The final number of BCC atoms is lower, because at higher temperature the simulation analysis tools find it more difficult to detect crystal structures. For the sample with ~ 5 million

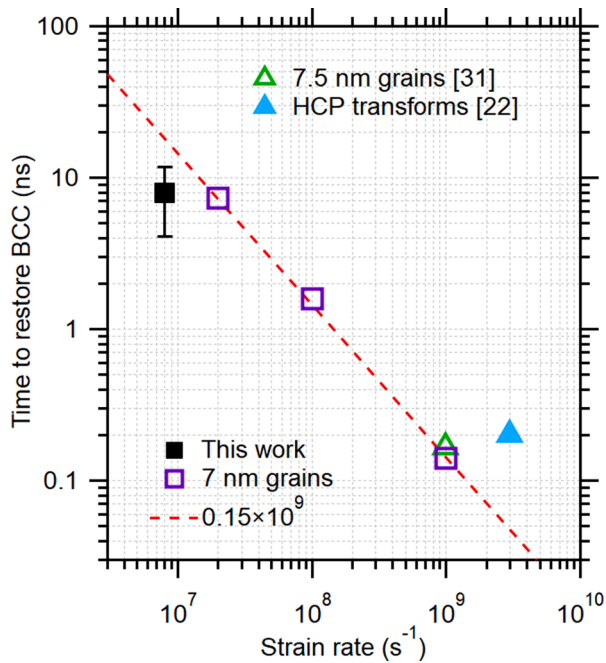


Fig. 5. Time to restore the BCC phase. Filled square is the experimental value and open symbols represent MD simulations from this work and the literature. Dashed line corresponds to fit for MD simulations of $\sim 10^8 \text{ s}^{-1}$ strain rate. Data from [22] are taken as the loss of HCP phase as lower-pressure phases were observed.

atoms and larger grain size there are no significant differences, and the percent of BCC atoms is only higher due to a smaller ratio of atoms in grain boundaries versus bulk material.

At the largest strain, all samples transform to HCP, with twins and stacking faults identified as FCC atoms (Fig. 6). Similar structures were obtained in previous works [29,31,33,37]. The unloading process leads to a BCC nanocrystal with almost the same grains as the un-deformed sample. This agrees with the experimental results of a microstructural memory effect, albeit at much different time and length scales. There is also evidence of dislocations and twins (Fig. S4) that are formed due to compression and are retained after release, which have also been observed in other computational work [29,33]. Additionally, there are no grain rotations, only misorientation due to twins and some grain boundary atoms. It is also observed that the dislocation density (ρ_{\perp}) from the simulations has a slight dependence on strain rate; for simulations at $2 \times 10^7 \text{ s}^{-1}$, 10^8 s^{-1} , and 10^9 s^{-1} , ρ_{\perp} is 0.68, 0.66, and $0.53 \times 10^{16} \text{ m}^{-2}$, respectively. Once again, these values are fairly consistent with previous work on spallation in iron [29,40].

4. Conclusions

The kinetics of the ε - α phase transition in pure iron driven to a pressure of 60 GPa and released at a free surface was studied using synchrotron x-ray diffraction. The spall strength was calculated based on velocimetry data, the phase and microstructural behavior were investigated with XRD measurements, and MD simulations were used to better understand the atomic-level behavior that occurs during the α - ε - α phase transformation pathway.

The following are the main findings of these experiments coupled with simulations:

- Spall strength of polycrystalline iron agrees with previous work on laser shock-induced spall. This suggests that the spallation mechanisms were similar as well; ductile failure occurred along grain boundaries following the complete α - ε - α phase transition cycle.

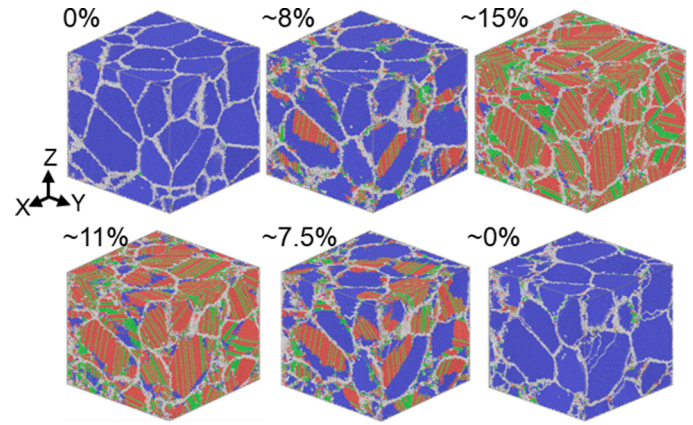


Fig. 6. Microstructural evolution of nanocrystalline simulations through (top row) compression and (bottom row) release as a function of percent strain. Colors represent structure. Red: HCP, Green: FCC, Blue: BCC, Gray: other. Note that OVITO labels stacking faults in HCP as FCC due to similar atomic plane ordering; thus, there is likely much less true FCC structure than is depicted in the 15% strain image. The evolution of atomic structure is similar for all strain rate cases simulated.

- The α - ε phase transition is observed during compression and is accompanied by a grain size reduction from the $\mu\text{-}$ to the nm- scale. Density is increased to $\sim 9 \text{ g/cm}^3$ before decompressing to an expanded structure, which can be attributed to temperature effects. Experiments and simulations give equivalent results.
- The volume-integrated reverse phase transition, ε - α , occurs during release prior to complete spall. This phase change at $\sim 10^6 \text{ s}^{-1}$ occurs within $\sim 8 \text{ ns}$ which is longer than previous experimental work on the subject (at higher strain rates) but is in agreement with the MD simulation of the experiment, which predict an inverse dependence of back-transformation time with strain rate.
- From the kinetic exponent in the JMAK model ($n \sim 1$), it can be concluded that the released α phase nucleates at grain boundaries. The rate constant, τ , can be further refined using a kinetic model that includes wave propagation physics.
- Experimental results also provide evidence of a microstructural memory effect where the grain size is reduced to the nm scale during compression and immediately starts to increase after the shock hits the free surface and begins release.
- MD simulations provide insight into the microstructural effects of shock compression and release, which include twins, stacking faults, dislocations. The initial grain structure, including size and orientation, is restored after complete unloading, in agreement with the experiments described here.

Future work might explore the role of initial sample temperature, grain texture and preexisting defects, like radiation-induced vacancies and voids or large dislocation densities from pre-strained samples, which might allow tailoring of the transformation kinetics.

Declaration of Competing Interest

The authors declare that they have no known competing financial interests or personal relationships that could have appeared to influence the work reported in this paper.

Acknowledgements

The work of GR, RJB, CVS, SS, SMC, RFS, RER, and HSP were supported by the U.S. Department of Energy, Lawrence Livermore National Laboratory, under Contract No. DE-AC52-07NA27344. Experimental work lead by GR was supported by LLNL ACT-UP grant (subcontract

B639114) and the Department of Energy, National Nuclear Security Administration under Award Number DE-NA0003842. EMB and OD thank support from PICTO-UUMM-2019-00048 and PIP2020-2022. This work used computational resources from CCAD – Universidad Nacional de Córdoba (<https://ccad.unc.edu.ar/>) and the Toko Cluster from FCEN-UNCuyo (<http://toko.uncu.edu.ar/>), which are part of SNCAD – Min-CyT, República Argentina. This publication is based upon work performed at the Dynamic Compression Sector, which is operated by Washington State University under the U.S. Department of Energy (DOE)/National Nuclear Security Administration award no. DE-NA0003957. This research used resources of the Advanced Photon Source; a DOE Office of Science User Facility operated for the DOE Office of Science by Argonne National Laboratory under contract no. DE-AC02-06CH11357. The technical staff at Sector 35, including Lee Wanatowicz, Adam Schumann, Nick Sinclair, Xiaoming Wang, Kory Green, Pinaki Das, Yuelin Li, is thanked for their assistance with conducting the laser shock experiments. This document is released as LLNL-JRNL-845223.

Supplementary materials

Supplementary material associated with this article can be found, in the online version, at [doi:10.1016/j.actamat.2023.119148](https://doi.org/10.1016/j.actamat.2023.119148).

References

- [1] H. Mao, W.A. Bassett, T. Takahashi, Effect of pressure on crystal structure and lattice parameters of iron up to 300 kbar, *J. Appl. Phys.* 38 (1967) 272–276, <https://doi.org/10.1063/1.1708965>.
- [2] P.M. Giles, M.H. Longenbach, A.R. Marder, High-pressure $\alpha \rightarrow \epsilon$ martensitic transformation in iron, *J. Appl. Phys.* 42 (1971) 4290–4295, <https://doi.org/10.1063/1.1659768>.
- [3] W.A. Bassett, E. Huang, Mechanism of the body-centered cubic–hexagonal close-packed phase transition in iron, *Science* 238 (1987) 780–783, <https://doi.org/10.1126/science.238.4828.780>.
- [4] R.D. Taylor, M.P. Pasternak, R. Jeanloz, Hysteresis in the high pressure transformation of bcc- to hcp-iron, *J. Appl. Phys.* 69 (1991) 6126–6128, <https://doi.org/10.1063/1.348779>.
- [5] F.M. Wang, R. Ingalls, Iron bcc-hcp transition: local structure from x-ray-absorption fine structure, *Phys. Rev. B* 57 (1998) 5647–5654, <https://doi.org/10.1103/PhysRevB.57.5647>.
- [6] J. Jiang, J.S. Olsen, L. Gerward, Grain-size and alloying effects on the pressure-induced bcc-to-hcp transition in nanocrystalline iron, *Mater. Trans.* 42 (2001) 1571–1574.
- [7] S. Merkel, H.R. Wenk, P. Gillet, H. Mao, R.J. Hemley, Deformation of polycrystalline iron up to 30 GPa and 1000 K, *Phys. Earth Planet. Inter.* 145 (2004) 239–251, <https://doi.org/10.1016/j.pepi.2004.04.001>.
- [8] Z. Konópková, A. Rothkirch, A.K. Singh, S. Speziale, H.P. Liermann, *In situ* x-ray diffraction of fast compressed iron: analysis of strains and stress under non-hydrostatic pressure, *Phys. Rev. B* 91 (2015), 144101, <https://doi.org/10.1103/PhysRevB.91.144101>.
- [9] S. Merkel, A. Lincot, S. Petitgirard, Microstructural effects and mechanism of bcc-hcp-bcc transformations in polycrystalline iron, *Phys. Rev. B* 102 (2020), 104103, <https://doi.org/10.1103/PhysRevB.102.104103>.
- [10] D.H. Kalantar, J.F. Belak, G.W. Collins, J.D. Colvin, H.M. Davies, J.H. Eggert, T. C. Germann, J. Hawreliak, B.L. Holian, K. Kadau, P.S. Lomdahl, H.E. Lorenzana, M. A. Meyers, K. Rosolankova, M.S. Schneider, J. Sheppard, J.S. Stölkén, J.S. Wark, Direct observation of the $\alpha - \epsilon$ transition in shock-compressed iron via nanosecond X-Ray diffraction, *Phys. Rev. Lett.* 95 (2005), 075502, <https://doi.org/10.1103/PhysRevLett.95.075502>.
- [11] J. Hawreliak, J.D. Colvin, J.H. Eggert, D.H. Kalantar, H.E. Lorenzana, J.S. Stölkén, H.M. Davies, T.C. Germann, B.L. Holian, K. Kadau, P.S. Lomdahl, A. Higginbotham, K. Rosolankova, J. Sheppard, J.S. Wark, Analysis of the x-ray diffraction signal for the $\alpha - \epsilon$ transition in shock-compressed iron: simulation and experiment, *Phys. Rev. B* 74 (2006), 184107, <https://doi.org/10.1103/PhysRevB.74.184107>.
- [12] S.J. Wang, M.L. Sui, Y.T. Chen, Q.H. Lu, E. Ma, X.Y. Pei, Q.Z. Li, H.B. Hu, Microstructural fingerprints of phase transitions in shock-loaded iron, *Sci. Rep.* 3 (2013) 1086, <https://doi.org/10.1038/srep01086>.
- [13] L.M. Dougherty, G.T. Gray III, E.K. Cerreta, R.J. McCabe, R.D. Field, J.F. Bingert, Rare twin linked to high-pressure phase transition in iron, *Scr. Mater.* 60 (2009) 772–775, <https://doi.org/10.1016/j.scriptamat.2009.01.014>.
- [14] N. Amadou, T. de Resseguier, E. Brambrink, T. Vinci, A. Benuzzi-Mounaix, G. Huser, G. Morard, F. Guyot, K. Miyazishi, N. Ozaki, R. Kodama, M. Koenig, Kinetics of the iron $\alpha - \epsilon$ phase transition at high-strain rates: experiment and model, *Phys. Rev. B* 93 (2016), 214108, <https://doi.org/10.1103/PhysRevB.93.214108>.
- [15] R.F. Smith, J.H. Eggert, D.C. Swift, J. Wang, T.S. Duffy, D.G. Braun, R.E. Rudd, D. B. Reisman, J.P. Davis, M.D. Knudson, G.W. Collins, Time-dependence of the alpha to epsilon phase transformation in iron, *J. Appl. Phys.* 114 (2013), 223507, <https://doi.org/10.1063/1.4839655>.
- [16] D. Bancroft, E.L. Peterson, S. Minshall, Polymorphism of iron at high pressure, *J. Appl. Phys.* 27 (1956) 291–298, <https://doi.org/10.1063/1.1722359>.
- [17] J.A. Hawreliak, D.H. Kalantar, J.S. Stölkén, B.A. Remington, H.E. Lorenzana, J. S. Wark, High-pressure nanocrystalline structure of a shock-compressed single crystal of iron, *Phys. Rev. B* 78 (2008), 220101, <https://doi.org/10.1103/PhysRevB.78.220101>.
- [18] S. Merkel, S. Hok, C. Bolme, D. Rittman, K.J. Ramos, B. Morrow, H.J. Lee, B. Nagler, E. Galtier, E. Granados, A. Hashim, W.L. Mao, A.E. Gleason, Femtosecond visualization of hcp-iron strength and plasticity under shock compression, *Phys. Rev. Lett.* 127 (2021), 205501, <https://doi.org/10.1103/PhysRevLett.127.205501>.
- [19] A.K. Zurek, M.A. Meyers, Microstructural aspects of dynamic failure. In: *High-Pressure Shock Compression of Solids II*, Springer, New York, NY, 1996, pp. 25–70.
- [20] T. de Resseguier, M. Hallouin, Effects of the $\alpha - \epsilon$ phase transition on wave propagation and spallation in laser shock-loaded iron, *Phys. Rev. B* 77 (2008), 174107, <https://doi.org/10.1103/PhysRevB.77.174107>.
- [21] L.M. Barker, R.E. Hollenbach, Shock wave study of the $\alpha \rightleftharpoons \epsilon$ phase transition in iron, *J. Appl. Phys.* 45 (1974) 4872–4887, <https://doi.org/10.1063/1.1663148>.
- [22] H. Hwang, E. Galtier, H. Cynn, I. Eom, S.H. Chun, Y. Bang, G.C. Hwang, J. Choi, T. Kim, M. Kong, S. Kwon, K. Kang, H.J. Lee, C. Park, J.I. Lee, Y. Lee, W. Yang, S. H. Shim, T. Vogt, S. Kim, J. Park, S. Kim, D. Nam, J.H. Lee, H. Hyun, M. Kim, T. Y. Koo, C.C. Kao, T. Sekine, Y. Lee, Subnanosecond phase transition dynamics in laser-shocked iron, *Sci. Adv.* 6 (2020) eaz5132, <https://doi.org/10.1126/sciadv.aaz5132>.
- [23] A. Dewaele, C. Denoual, S. Anzellini, F. Occelli, M. Mezour, P. Cordier, S. Merkel, M. Wéaech, E. Rausch, Mechanism of the $\alpha - \epsilon$ phase transformation in iron, *Phys. Rev. B* 91 (2015), 174105, <https://doi.org/10.1103/PhysRevB.91.174105>.
- [24] J.A. Hawreliak, S.J. Turneaure, Probing the lattice structure of dynamically compressed and released single crystal iron through the alpha to epsilon phase transition, *J. Appl. Phys.* 129 (2021), 135901, <https://doi.org/10.1063/5.0042605>.
- [25] J.C. Boettger, D.C. Wallace, Metastability and dynamics of the shock-induced phase transition in iron, *Phys. Rev. B* 55 (1997) 2840–2849, <https://doi.org/10.1103/PhysRevB.55.2840>.
- [26] K. Kadau, T.C. Germann, P.S. Lomdahl, B.L. Holian, Atomistic simulations of shock-induced transformations and their orientation dependence in bcc Fe single crystals, *Phys. Rev. B* 72 (2005), 064120, <https://doi.org/10.1103/PhysRevB.72.064120>.
- [27] B.J. Jensen, G.T. Gray, R.S. Hixson, Direct measurements of the α - ϵ transition stress and kinetics for shocked iron, *J. Appl. Phys.* 105 (2009), 103502, <https://doi.org/10.1063/1.3110188>.
- [28] N. Amadou, T. de Resseguier, A. Dragon, E. Brambrink, Coupling between plasticity and phase transition in shock- and ramp-compressed single-crystal iron, *Phys. Rev. B* 98 (2018), 024104, <https://doi.org/10.1103/PhysRevB.98.024104>.
- [29] K. Ma, A.M. Dongare, Role of $\alpha \rightarrow \epsilon \rightarrow \alpha$ phase transformation on the spall behavior of iron at atomic scales, *J. Mater. Sci.* 57 (2022) 12556–12571, <https://doi.org/10.1007/s10853-022-07381-8>.
- [30] N. Gunkelmann, E.M. Bringa, H.M. Urbassek, Influence of phase transition on shock-induced spallation in nanocrystalline iron, *J. Appl. Phys.* 118 (2015), 185902, <https://doi.org/10.1063/1.4935452>.
- [31] H.T. Luu, R.J. Ravelo, M. Rudolph, E.M. Bringa, T.C. Germann, D. Rafaja, N. Gunkelmann, Shock-induced plasticity in nanocrystalline iron: large-scale molecular dynamics simulations, *Phys. Rev. B* 102 (2020), 020102, <https://doi.org/10.1103/PhysRevB.102.020102>.
- [32] K. Kadau, T.C. Germann, P.S. Lomdahl, R.C. Albers, J.S. Wark, A. Higginbotham, B. L. Holian, Shock waves in polycrystalline iron, *Phys. Rev. Lett.* 98 (2007), 135701, <https://doi.org/10.1103/PhysRevLett.98.135701>.
- [33] N. Gunkelmann, D.R. Tramontina, E.M. Bringa, H.M. Urbassek, Morphological changes in polycrystalline Fe after compression and release, *J. Appl. Phys.* 117 (2015), 085901, <https://doi.org/10.1063/1.4913622>.
- [34] H.T. Luu, R.G.A. Veiga, N. Gunkelmann, Atomistic study of the role of defects on $\alpha - \epsilon$ phase transformations in iron under hydrostatic compression, *Metals (Basel)* 9 (2019) 1040, <https://doi.org/10.3390/met9101040>.
- [35] X.X. Guo, J.L. Shao, G. Lu, Reversibility of the structural transition in single crystal iron driven by uniaxial and triaxial strains: atomistic study, *Int. J. Mech. Sci.* 191 (2021), 106064, <https://doi.org/10.1016/j.ijmecsci.2020.106064>.
- [36] N. Gunkelmann, E.M. Bringa, K. Kang, G.J. Ackland, C.J. Ruestes, H.M. Urbassek, Polycrystalline iron under compression: plasticity and phase transitions, *Phys. Rev. B* 86 (2012), 144111, <https://doi.org/10.1103/PhysRevB.86.144111>.
- [37] J. Hu, X. Liu, T. Mashimo, J. Zhang, G. Luo, Y. Sun, Q. Shen, H. Huang, L. Zhang, Experimental and atomic observations of phase transformations in shock-compressed single-crystal Fe, *Materialia* 20 (2021), 101200, <https://doi.org/10.1016/j.mtla.2021.101200>.
- [38] X. Wang, P. Rigg, J. Sethian, N. Sinclair, N. Weir, B. Williams, J. Zhang, J. Hawreliak, Y. Toyoda, Y. Gupta, Y. Li, D. Broege, J. Bromage, R. Earley, D. Guy, J. Zuegel, The laser shock station in the dynamic compression sector. I, *Rev. Sci. Instrum.* 90 (2019), 053901, <https://doi.org/10.1063/1.5088367>.
- [39] R.B. Von Dreele, S.M. Clarke, J.P.S. Walsh, 'Pink'-beam X-ray powder diffraction profile and its use in Rietveld refinement, *J. Appl. Crystallogr.* 54 (2021) 3–6, <https://doi.org/10.1107/S1600576720014624>.
- [40] G. Righi, C.J. Ruestes, C.V. Stan, S.J. Ali, R.E. Rudd, M. Kawasaki, H.S. Park, M. A. Meyers, Towards the ultimate strength of iron: spalling through laser shock, *Acta Mater.* 215 (2021), 117072, <https://doi.org/10.1016/j.actamat.2021.117072>.
- [41] D. Dolan, Foundations of VISAR analysis., 2006. 10.2172/886901.

- [42] P.M. Celliers, D.K. Bradley, G.W. Collins, D.G. Hicks, T.R. Boehly, W.J. Armstrong, Line-imaging velocimeter for shock diagnostics at the OMEGA laser facility, *Rev. Sci. Instrum.* 75 (2004) 4916–4929, <https://doi.org/10.1063/1.1807008>.
- [43] Inertial Confinement Fusion Quarterly report, April–June 1995, Lawrence Livermore National Lab., CA (United States), 1995, <https://doi.org/10.2172/187252>. Volume 5, No. 3.
- [44] C. Prescher, V.B. Prakapenka, DIOPTAS: a program for reduction of two-dimensional X-ray diffraction data and data exploration, *High Press Res* 35 (2015) 223–230, <https://doi.org/10.1080/08957959.2015.1059835>.
- [45] B.H. Toby, R.B. Von Dreele, GSAS-II: the genesis of a modern open-source all purpose crystallography software package, *J. Appl. Crystallogr.* 46 (2013) 544–549, <https://doi.org/10.1107/S0021889813003531>.
- [46] A.P. Thompson, H.M. Aktulga, R. Berger, D.S. Bolintineanu, W.M. Brown, P. S. Crozier, P.J. In 'T Veld, A. Kohlmeyer, S.G. Moore, T.D. Nguyen, R. Shan, M. J. Stevens, J. Tranchida, C. Trott, S.J. Plimpton, LAMMPS - a flexible simulation tool for particle-based materials modeling at the atomic, meso, and continuum scales, *Comput. Phys. Commun.* 271 (2022), 108171, <https://doi.org/10.1016/j.cpc.2021.108171>.
- [47] P. Hirel, Atoms: a tool for manipulating and converting atomic data files, *Comput. Phys. Commun.* 197 (2015) 212–219, <https://doi.org/10.1016/j.cpc.2015.07.012>.
- [48] A. Stukowski, Visualization and analysis of atomistic simulation data with OVITO—the open visualization tool, *Modelling Simul. Mater. Sci. Eng.* 18 (2010), 015012, <https://doi.org/10.1088/0965-0393/18/1/015012>.
- [49] P.M. Larsen, S. Schmidt, J. Schiøtz, Robust structural identification via polyhedral template matching, *Modell. Simul. Mater. Sci. Eng.* 24 (2016), 055007, <https://doi.org/10.1088/0965-0393/24/5/055007>.
- [50] T. Antoun (Ed.), *Spall Fracture*, Springer, New York, 2003.
- [51] M.A. Meyers, *Dynamic Behavior of Materials*, John Wiley & Sons, 1994.
- [52] H. Shu, X. Huang, H. Pan, J. Ye, F. Zhang, G. Jia, Z. Fang, Y. Tu, Z. Xie, S. Fu, Plastic behavior of steel and iron in high strain rate regime, *Int. J. Fract.* 206 (2017) 81–93, <https://doi.org/10.1007/s10704-017-0202-6>.
- [53] D. Curran, Dynamic failure of solids, *Phys. Rep.* 147 (1987) 253–388, [https://doi.org/10.1016/0370-1573\(87\)90049-4](https://doi.org/10.1016/0370-1573(87)90049-4).
- [54] T.P. Remington, E.N. Hahn, S. Zhao, R. Flanagan, J.C.E. Mertens, S. Sabbaghianrad, T.G. Langdon, C.E. Wehrenberg, B.R. Maddox, D.C. Swift, B. A. Remington, N. Chawla, M.A. Meyers, Spall strength dependence on grain size and strain rate in tantalum, *Acta Mater.* 158 (2018) 313–329, <https://doi.org/10.1016/j.actamat.2018.07.048>.
- [55] H. Jarmakani, B. Maddox, C.T. Wei, D. Kalantar, M.A. Meyers, Laser shock-induced spalling and fragmentation in vanadium, *Acta Mater.* 58 (2010) 4604–4628, <https://doi.org/10.1016/j.actamat.2010.04.027>.
- [56] S.A. Thomas, M.C. Hawkins, M.K. Matthes, G.T. Gray, R.S. Hixson, Dynamic strength properties and alpha-phase shock Hugoniot of iron and steel, *J. Appl. Phys.* 123 (2018), 175902, <https://doi.org/10.1063/1.5019484>.
- [57] J. Wang, R.F. Smith, J.H. Eggert, D.G. Braun, T.R. Boehly, J.R. Patterson, P. M. Celliers, R. Jeanloz, G.W. Collins, T.S. Duffy, Ramp compression of iron to 273 GPa, *J. Appl. Phys.* 114 (2013), 023513, <https://doi.org/10.1063/1.4813091>.
- [58] S.V. Razorenov, G.I. Kanel, V.E. Fortov, Iron at high negative pressures, *JETP Lett.* 80 (2004) 348–350, <https://doi.org/10.1134/1.1825120>.
- [59] E.B. Zaretsky, G.I. Kanel, Yield stress, polymorphic transformation, and spall fracture of shock-loaded iron in various structural states and at various temperatures, *J. Appl. Phys.* 117 (2015), 195901, <https://doi.org/10.1063/1.4921356>.
- [60] G.V. Garkushin, N.S. Naumova, S.A. Atroshenko, S.V. Razorenov, Influence of the reversible α - ϵ phase transition and preliminary shock compression on the spall strength of armco iron, *Tech. Phys.* 61 (2016) 84–90, <https://doi.org/10.1134/S1063784216010102>.
- [61] G.I. Kanel, S.V. Razorenov, G.V. Garkushin, S.I. Ashitkov, P.S. Komarov, M. B. Agranat, Deformation resistance and fracture of iron over a wide strain rate range, *Phys. Solid State.* 56 (2014) 1569–1573, <https://doi.org/10.1134/S1063783414080113>.
- [62] H.M. Rietveld, A profile refinement method for nuclear and magnetic structures, *J. Appl. Crystallogr.* 2 (1969) 65–71, <https://doi.org/10.1107/S0021889869006558>.
- [63] W. Johnson, R. Mehl, Reaction kinetics in processes of nucleation and growth, *Trans. Metal. Soc.* 135 (1939) 416–442.
- [64] M. Avrami, Kinetics of phase change. I general theory, *J. Chem. Phys.* 7 (1939) 1103–1112, <https://doi.org/10.1063/1.1750380>.
- [65] A.N. Kolmogorov, On the statistical theory of the crystallization of metals, *Bull. Acad. Sci. USSR Math. Ser.* 1 (1937) 355–359.
- [66] M.G. Gorman, D. McGonagle, S.J. Tracy, S.M. Clarke, C.A. Bolme, A.E. Gleason, S. J. Ali, S. Hok, C.W. Greeff, P.G. Heighway, K. Hulpach, B. Glam, E. Galtier, H. J. Lee, J.S. Wark, J.H. Eggert, J.K. Wicks, R.F. Smith, Recovery of a high-pressure phase formed under laser-driven compression, *Phys. Rev. B.* 102 (2020), 024101, <https://doi.org/10.1103/PhysRevB.102.024101>.
- [67] A.E. Gleason, C.A. Bolme, E. Galtier, H.J. Lee, E. Granados, D.H. Dolan, C.T. Seagle, T. Ao, S. Ali, A. Lazicki, D. Swift, P. Celliers, W.L. Mao, Compression freezing kinetics of water to ice VII, *Phys. Rev. Lett.* 119 (2017), 025701, <https://doi.org/10.1103/PhysRevLett.119.025701>.
- [68] M. Avrami, Kinetics of phase change. II transformation-time relations for random distribution of nuclei, *J. Chem. Phys.* 8 (1940) 212–224, <https://doi.org/10.1063/1.1750631>.
- [69] P. Scherrer, *Nachr Ges wiss goettingen, Math. Phys.* 2 (1918) 98–100.
- [70] P.G. Heighway, M. Sliwa, D. McGonagle, C. Wehrenberg, C.A. Bolme, J. Eggert, A. Higginbotham, A. Lazicki, H.J. Lee, B. Nagler, H.S. Park, R.E. Rudd, R.F. Smith, M.J. Suggit, D. Swift, F. Tavella, B.A. Remington, J.S. Wark, Nonisentropic release of a shocked solid, *Phys. Rev. Lett.* 123 (2019), 245501, <https://doi.org/10.1103/PhysRevLett.123.245501>.